# Vortex propagation and phase transitions in a chiral antiferromagnetic nanostripe

Riccardo Tomasello [1] and Stavros Komineas [1,2]

[1] *Institute of Applied and Computational Mathematics, FORTH, 70013 Heraklion, Crete, Greece*

[2] *Department of Mathematics and Applied Mathematics, University of Crete, 70013 Heraklion, Crete, Greece*

(Received 9 January 2021; accepted 10 August 2021; published 23 August 2021)

We study a vortex in a nanostripe of an antiferromagnet with easy-plane anisotropy and interfacial Dzyaloshinskii-Moriya interaction. The vortex has hybrid chirality, being of Néel type close to its center and of Bloch type away from it. Propagating vortices can acquire velocities up to a maximum value that is lower than the spin wave velocity. Theoretical arguments lead to the general result that the velocity of localized excitations in chiral antiferromagnets cannot reach the spin wave velocity. When the vortex is forced to exceed the maximum velocity, phase transitions occur to a nonflat spiral, vortex chain, and flat spiral, successively. The vortex chain is a topological configuration stabilized in the stripe geometry.

DOI: 10.1103/PhysRevB.104.064438

## I. INTRODUCTION

A wide range of materials present antiferromagnetic order, where neighboring magnetic moments are coupled via a strong exchange interaction and are aligned in an antiparallel manner. Antiferromagnets (AFMs) exhibit features, such as low magnetic susceptibility, robustness against external fields, and lack of stray fields, that are favorable for the building blocks of spintronic devices [1,2]. They receive renewed interest because current techniques allow for the antiferromagnetic order to be manipulated by spin currents and to be observed despite the lack of net magnetization [3–8]. This opens the way for a number of potential applications including storage with picosecond switching [9–11], terahertz oscillators [12–14], racetrack memory based on magnetic solitons such as domain walls (DWs) [15–17], or skyrmions [18–21], which can achieve velocities larger than 1 km/s [15,16,21].

Some AFM materials such as $\alpha$-$Fe_2O_3$ and $Ba_2CuFe_2O_7$ are characterized by easy-plane anisotropy, which supports the formation of vortices. The latter have been discussed theoretically in infinite films [22–26] and observed experimentally by imprinting techniques [27,28] and, more recently, by x-ray magnetic linear dichroism combined with photoemission electron microscopy (XMLD-PEEM) [29]. Despite this, they have received much less attention than DWs or skyrmions or even than their ferromagnetic counterparts [30–37].

An extensive experimental investigation of an easy-plane AFM with the Dzyaloshinskii-Moriya interaction (DMI) established spiral antiferromagnetic order [38,39], and a subsequent theoretical analysis has shown the existence of two spiral phases [40,41]. For weak DMI, the Néel state is the ground state, but for stronger DMI the system enters a spiral phase where all Néel vector components vary in space (nonflat spiral). Only for strong enough DMI, the Néel vector lies in a plane and rotates in space, thus giving a flat spiral. The nonflat spiral gives an intermediate phase that is not there in the case of an easy-axis magnet [42].

We study theoretically vortices in easy-plane AFMs with an interfacial DMI. We consider a stripe geometry as this is the most suitable for applications involving shifting of magnetic information, while it will also give rise to interesting effects on the magnetic structure. We calculate the magnetic ground state and demonstrate that this induces a vortex with a mixed chirality, i.e., Néel-type chirality near the vortex core and Bloch-type chirality away from it. This unusual type of vortex will be referred to as a *hybrid* vortex.

We subsequently study propagating vortices. Despite the lack of Lorentz invariance due to the DMI, the propagating vortex exhibits Lorentz-like contraction in the direction of propagation, similarly to AFM DWs [16], but it elongates along the perpendicular direction, similarly to AFM skyrmions [21,43]. The vortex can acquire a maximum velocity beyond which it becomes unstable to periodic configurations, thus giving rise successively to a nonflat spiral, a vortex chain, and a flat spiral. The spirals are extensions of states known within the one-dimensional model, but the vortex chain is a feature of the stripe geometry. A theoretical explanation for the dynamical behavior is obtained, and it leads to the general result that the velocity of localized excitations in chiral AFMs cannot reach the spin wave velocity. Our results provide an understanding of the statics and dynamics of vortices in chiral AFMs and could stimulate additional studies, including the specific effect of spin torques, for the design of antiferromagnetic devices based on magnetic solitons.

This paper is organized as follows. In Sec. II, we introduce the model and review the one-dimensional spiral phases. In Sec. III we introduce vortex solutions in a stripe geometry. In Sec. IV, we find numerically and discuss propagating vortices and phase transitions to periodic states. Section V contains our concluding remarks. In Appendix A, we give the ground state of a one-dimensional chiral system with boundaries. The results are used for the understanding of the form of the hybrid vortex in Sec. III and of the phase transitions in Sec. IV. In Appendix B, we prove that a traveling domain wall cannot reach the velocity of spin waves; the results of Sec. IV are based on arguments similar to the argument developed in Appendix B. In Appendix C we show the equivalence of open and natural

 

boundary conditions for the chiral system. The results are used to support the validity of our numerical simulations.

## II. THE MODEL AND GROUND STATES

We consider an antiferromagnetic nanostripe with exchange, interfacial DMI, and easy-plane anisotropy. A continuum model is obtained for the normalized Néel vector $\boldsymbol{n} = (n_1, n_2, n_3)$, where $1, 2, 3$ refer to the $x, y, z$ directions, respectively, with the potential energy [26,44]

$$V = \int \left[\frac{1}{2}(\partial_\mu \boldsymbol{n}) \cdot (\partial_\mu \boldsymbol{n}) - \lambda \epsilon_{\mu\nu} \hat{\boldsymbol{e}}_\mu \cdot (\partial_\nu \boldsymbol{n} \times \boldsymbol{n}) + \frac{1}{2} n_3^2\right] dxdy, \tag{1}$$

where $\mu$, $\nu$ take the values 1,2, $\epsilon_{\mu\nu}$ is the totally antisymmetric tensor, $\hat{\boldsymbol{e}}_\mu$ denote the unit vectors in the respective directions, and $\lambda$ is a scaled DMI parameter. The equation of motion is

$$\boldsymbol{n} \times (\ddot{\boldsymbol{n}} - \boldsymbol{f}) = 0,$$
$$\boldsymbol{f} = \Delta \boldsymbol{n} + 2\lambda \epsilon_{\mu\nu} \hat{\boldsymbol{e}}_\mu \times \partial_\nu \boldsymbol{n} - n_3 \hat{\boldsymbol{e}}_3. \tag{2}$$

The unit of length used in this equation is the domain wall width. It is straightforward to check that Lorentz invariance is broken due to the presence of the DMI in Eq. (2). This fact underlies some of the main results discussed in this paper.

Let us review the results for a one-dimensional (1D) model with the energy (1) and $\boldsymbol{n} = \boldsymbol{n}(x)$. Phase transitions occur at the two critical values of the parameter [40]

$$\lambda_{NF} = \tfrac{1}{2}, \quad \lambda_F \approx 0.705. \tag{3}$$

We give schematically the three regimes separated by the critical values of $\lambda$.

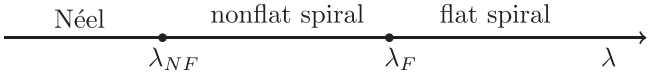


For weak DMI, $\lambda < \lambda_{NF}$, the Néel state is the ground state (see Ref. [45] for a related model). The Néel vector lies in the easy plane, and for definiteness we will assume $\boldsymbol{n} = \hat{\boldsymbol{e}}_2$. Increasing $\lambda$, we enter an intermediate phase in the form of a nonflat spiral at $\lambda = \lambda_{NF}$. The spiral presents a continuous rotation of the projection of $\boldsymbol{n}$ on the (13) plane as we move along the $x$ axis and, at the same time, the component $n_2$ oscillates around a nonzero value. The period of the spiral tends to infinity for $\lambda \to \lambda_{NF}$, while the component $n_2 \to 1$ in the same limit. As $\lambda$ increases, $n_2$ decreases, and it vanishes at $\lambda = \lambda_F$ where a flat spiral is obtained with $\boldsymbol{n}$ lying fully and rotating on the (13) plane. For $\lambda > \lambda_F$, the flat spiral remains the ground state, and the period of the spiral decreases with increasing $\lambda$ [40,45].

## III. VORTEX IN A STRIPE

Let us now assume a stripe geometry. This has a width $w$ in the $y$ direction, $-w/2 \leqslant y \leqslant w/2$, and it is much longer in the $x$ direction. We focus on the regime $\lambda < \lambda_{NF}$, where we expect a Néel state. Any solution of Eq. (2) should satisfy the natural boundary condition

$$\partial_y \boldsymbol{n} + \lambda \hat{\boldsymbol{e}}_1 \times \boldsymbol{n} = 0, \quad y = \pm \frac{w}{2}. \tag{4}$$

In the finite interval $-w/2 < y < w/2$, two degenerate nontrivial ground states with negative energy can be found, as shown in Appendix A. We denote these $\boldsymbol{n} = \boldsymbol{n}_\pm$, and $\boldsymbol{n}$ is primarily aligned along $\pm\hat{\boldsymbol{e}}_2$. In the case of the stripe, we extend the previous 1D configuration in the $x$ direction, and we have two degenerate ground states where $\boldsymbol{n}$ does not depend on $x$, that is, $\boldsymbol{n}(x, y) = \boldsymbol{n}_\pm(y)$. This is a quasiuniform state where the Néel vector points primarily along $\pm\hat{\boldsymbol{e}}_2$ and it tilts out of the plane, in $\hat{\boldsymbol{e}}_3$, in the regions close to the boundaries $y = \pm w/2$. Effectively, the boundary condition (4) makes $\hat{\boldsymbol{e}}_2$ an energetically favorable axis.

We simulate the system numerically on a stripe domain with a long $x$ dimension, which typically contains 1000 grid points with lattice spacing 0.1, giving a physical dimension of 100. We vary the width of the stripe. We impose Neumann boundary conditions at the ends of the numerical mesh in the $x$ direction. In the $y$ direction, we use open boundary conditions at $y = \pm w/2$. (In Appendixes A and C, it is shown that these give the same results as the natural boundary conditions). A relaxation algorithm indeed converges to a quasiuniform state of the form $\boldsymbol{n} = \boldsymbol{n}_\pm(y)$, which does not depend on $x$.

Vortices should be excited states on the quasiuniform state in the regime $\lambda < \lambda_{NF}$. Due to the form of the DMI, a vortex solution of model (2) is expected to be of Néel type in an infinite film. The form of the ground state forces us to assume in-plane domains oriented primarily along $\pm\hat{\boldsymbol{e}}_2$ on the left and right side of the stripe, respectively, i.e., $\boldsymbol{n}(x \to \pm\infty, y) = \boldsymbol{n}_\pm(y)$, separated by an out-of-plane domain wall in the center of the stripe. This ansatz is used as an initial condition in our numerical relaxation method. We run simulations for different widths $w$ and parameter values $\lambda$. The parameter is given as $\lambda = D/(2\sqrt{AK})$, where $A$, $D$, and $K$ are the exchange, DMI, and anisotropy constants in physical units. Considering $A = 14$ pJ/m [29] and $K = 5$ kJ/m$^3$ [46], we obtain $\lambda = 0.3$ for $D = 0.16$ mJ/m$^2$. A vortex is obtained as an equilibrium state for stripes with width larger than a critical width that depends on $\lambda$. For $w > 4$, we obtain a vortex for all values of $\lambda$.

Figure 1 shows the results of simulations on a $1000 \times 100$ grid with lattice spacing 0.1, giving physical dimensions $100 \times 10$ (in domain wall width units). Figures 1(a), 1(b), and 1(c) show vector plots of a static vortex in a stripe with $w = 10$ for three values of the DMI parameter $\lambda = 0.2$, 0.3, and 0.4, respectively. The vortex is of Néel type close to the vortex core, and it gradually becomes of Bloch type as we go away from the core, thus exhibiting a hybrid character. Starting from the vortex core, the Néel vector goes towards the in-plane direction by rotating in the (13) plane as well as in the (23) plane. This results in a vortex configuration which is between Néel and Bloch types near the vortex core, similar to what happens with Dzyaloshinskii DWs [47] or skyrmions with intermediate chirality [48,49]. The (13) rotation is a consequence of the interfacial DMI, while the (23) rotation is a consequence of the boundary conditions which force the Néel vector to be oriented primarily along $\hat{\boldsymbol{e}}_2$ in the far field. As we move farther from the vortex core, the magnetization becomes aligned with $\pm\hat{\boldsymbol{e}}_2$ in opposite directions on the left and right sides of the stripe.

Figures 1(d), 1(e), and 1(f) show the Néel vector profiles along the line in the center of the stripe, $y = 0$, corresponding to the vortices in Figs. 1(a), 1(b), and 1(c), respectively.

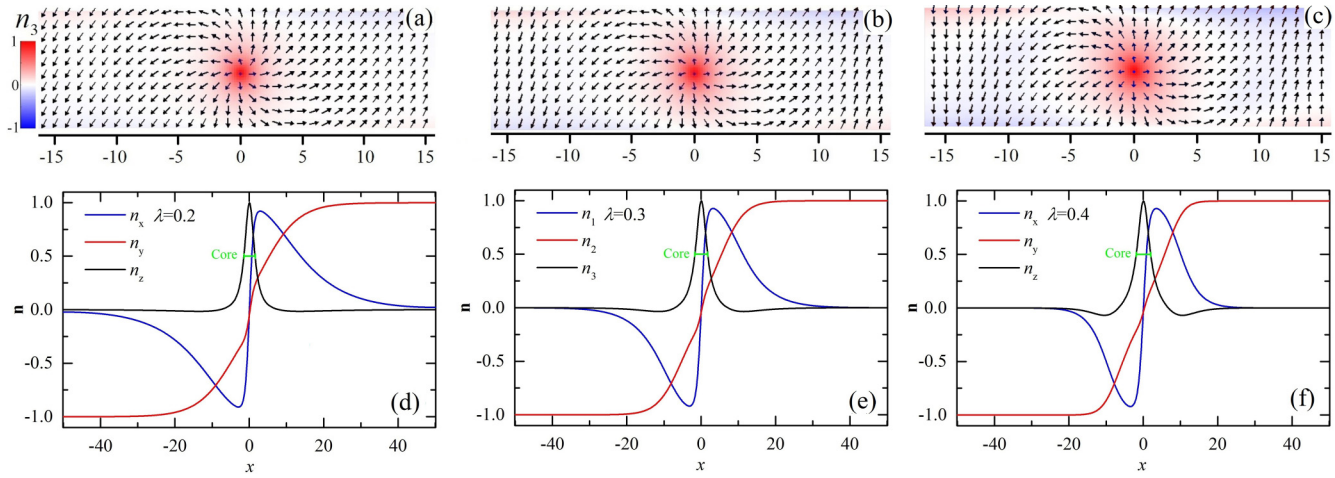


FIG. 1. Static hybrid vortex in a stripe that lies on the $xy$ plane. The stripe width $w$ is 10 (in the $y$ direction) and the length $L = 100$ (in the $x$ direction) in domain wall width units. (a)–(c) Vector plots of the static hybrid vortex for three values of the DMI parameter. Vectors show the projection of the Néel vector on the plane $(n_1, n_2)$, while the component $n_3$ is shown by a color scale. (d)–(f) The components of $\boldsymbol{n}$ along the line in the center of the stripe ($y = 0$) for the configurations shown in (a)–(c). The vortex core width is shown by a green solid line.

Increasing the DMI parameter has two main effects: (i) an increase of the vortex core width $L_0$ defined as the distance between the positions where $n_3 = 0.5$, as also noted in the Appendix of Ref. [40], and (ii) a faster rotation of the Néel vector towards $\hat{\boldsymbol{e}}_2$.

The vortex energy is finite in a stripe, in contrast to the logarithmically diverging vortex energy in infinite films. The vortex energy above the ground state as a function of the stripe width $w$ is shown in Fig. 2. We find numerically a Néel-type vortex in the same stripe geometries by starting our relaxation simulations with a Néel vortex as an initial state. Its energy, shown in Fig. 2, is higher than the energy of the hybrid vortex for the whole range of stripe widths $w$.

## IV. PROPAGATING VORTEX

We proceed to study the dynamics of the hybrid vortex. Let us assume that a magnetic configuration is set into motion

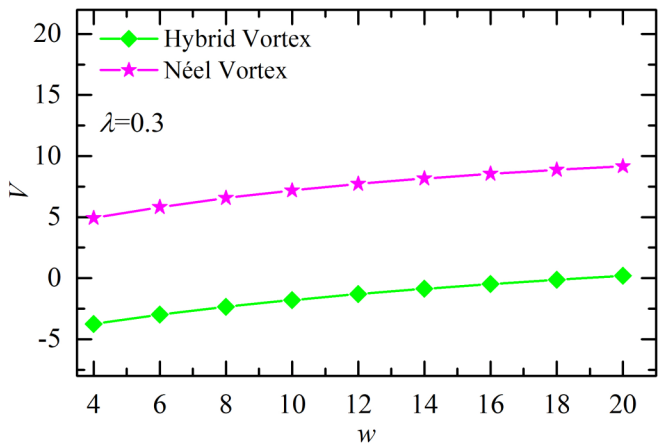


FIG. 2. Energy $V$ above the ground-state energy as a function of the stripe width $w$ for the hybrid vortex and for the Néel vortex for $\lambda = 0.3$. The numerical results are given by symbols (rhombus, star) connected by solid lines.

and we obtain a configuration $\boldsymbol{n}(\xi)$, $\xi = x - vt$, propagating along the axis of the stripe. This is substituted into Eq. (2), which takes the form

$$\boldsymbol{n}\times\big[(1-v^2)\partial_1^2\boldsymbol{n} + \partial_2^2\boldsymbol{n} + 2\lambda(\hat{\boldsymbol{e}}_1\times\partial_2\boldsymbol{n} - \hat{\boldsymbol{e}}_2\times\partial_1\boldsymbol{n}) - n_3\hat{\boldsymbol{e}}_3\big] = 0. \tag{5}$$

Applying a rescaling $\xi \to \xi\sqrt{1-v^2}$, we get

$$\boldsymbol{n}\times\left[\partial_1^2\boldsymbol{n} + \partial_2^2\boldsymbol{n} + 2\lambda\left(\hat{\boldsymbol{e}}_1\times\partial_2\boldsymbol{n} - \frac{1}{\sqrt{1-v^2}}\hat{\boldsymbol{e}}_2\times\partial_1\boldsymbol{n}\right) - n_3\hat{\boldsymbol{e}}_3\right] = 0. \tag{6}$$

In the following, we will find propagating vortices as solutions of the latter equation. Equation (6) contains the velocity $v$ in one of the DMI terms, and it cannot be reduced to a static form.

In order to make progress analytically, we initially neglect the dependence on $y$, and Eq. (6) reduces to

$$\boldsymbol{n}\times\left(\partial_1^2\boldsymbol{n} - 2\frac{\lambda}{\sqrt{1-v^2}}\hat{\boldsymbol{e}}_2\times\partial_1\boldsymbol{n} - n_3\hat{\boldsymbol{e}}_3\right) = 0, \tag{7}$$

where a single combination of parameters appears. The phases of this 1D system were reviewed in Sec. II. We have the following three cases: (a) the Néel state for

$$\frac{\lambda}{\sqrt{1-v^2}} < \lambda_{NF} \Rightarrow v < \sqrt{1-\left(\frac{\lambda}{\lambda_{NF}}\right)^2} \equiv v_{NF}, \tag{8}$$

(b) the nonflat spiral for

$$\lambda_{NF} < \frac{\lambda}{\sqrt{1-v^2}} < \lambda_F \Rightarrow \sqrt{1-\left(\frac{\lambda}{\lambda_{NF}}\right)^2} < v < \sqrt{1-\left(\frac{\lambda}{\lambda_F}\right)^2}, \tag{9}$$

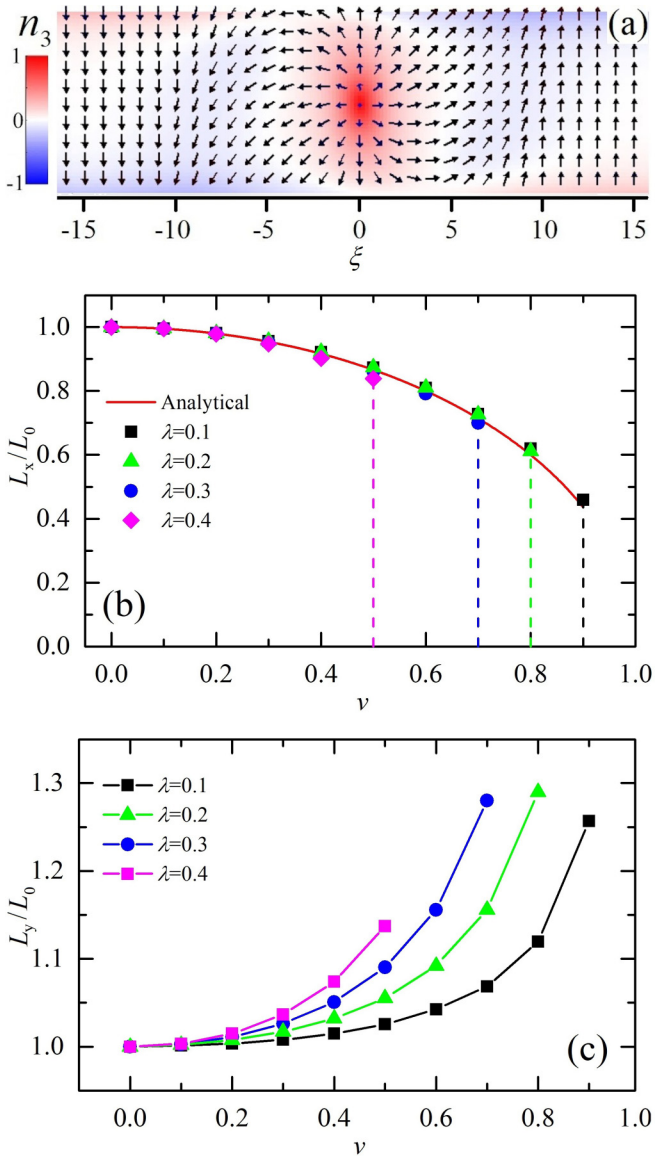


FIG. 3. (a) Vector plot for $\lambda = 0.4$ for the propagating hybrid vortex for velocity $v = 0.60$. Plotting conventions are as in Fig. 1. (b) Vortex core width $L_x$ in the direction of propagation for a propagating vortex as a function of velocity $v$, for various values of $\lambda$, normalized to the width of a static vortex $L_0$. The red solid line shows the expected result for Lorentz-type contraction $L_x = \sqrt{1 - v^2}$. The dashed lines mark the maximum obtained velocities for the respective $\lambda$ values. (c) Vortex core width $L_y$ in the $y$ axis for the propagating vortex as a function of velocity $v$, normalized to the width of a static vortex $L_0$.

and (c) the flat spiral for

$$\frac{\lambda}{\sqrt{1-v^2}} > \lambda_F \Rightarrow v > \sqrt{1-\left(\frac{\lambda}{\lambda_F}\right)^2} \equiv v_F. \qquad (10)$$

Using a numerical relaxation method [43] applied to Eq. (6), we find hybrid vortices in a steady-state motion propagating along the axis of the stripe with a range of velocities $v$. Figure 3(a) shows a propagating vortex with velocity $v = 0.6$. Starting from the static hybrid vortex and increasing $v$, we find that the propagating vortex is contracted along the $x$ direction and it is elongated along the $y$ direction. A propagating vortex (or soliton) has a nonzero local magnetization [43], in contrast to a static one. This feature may prove crucial for applications such as magnet-superconductor hybrids, where skyrmions and vortices are found to serve as potential hosts to Majorana bound states [50–52].

Figure 3(b) shows the width $L_x$ of the propagating vortex in the $x$ axis as a function of velocity for various values of $\lambda$, normalized to the width $L_0$ of the static vortex. The width $L_x$, in the direction of propagation, closely follows the law of Lorentz-type contraction (shown by a solid line in the figure) despite the fact that the model is not Lorentz invariant. Lorentz contraction is exactly followed by a propagating DW as reported in Ref. [16] and reviewed in Appendix B. For each $\lambda$, the vortex achieves a maximum velocity (marked by dashed lines) as we explain below. Therefore there is a minimum achievable vortex width which decreases with decreasing $\lambda$. Figure 3(c) shows the width $L_y$ of the vortex core in the $y$ direction. It increases with the velocity, making the vortex elongation increasingly pronounced.

When the velocity exceeds the value $v_{NF}(\lambda)$ in Eq. (8), we expect a nonflat spiral to develop based on the reasoning given following Eq. (7). The numerical simulations show that this actually happens in the case of the stripe at a higher velocity. Figure 4(a) shows the nonflat spiral that is nucleated, for $\lambda = 0.4$, when a single vortex is set into motion with a velocity $v = 0.78$. The vortex has survived in the stripe center, and it is strongly elongated in the $y$ direction. Figure 4(d) shows line plots of the Néel vector components along the line $y = 0$ in the center of the stripe. The spiral configuration is obvious in the $n_1$ and $n_3$ components. The component $n_2$ oscillates around nonzero values with opposite signs on the two sides of the vortex. The configuration has the features of a DW on top of a spiral state (or a defect in the periodic structure). Such a DW is connecting two topologically distinct spatially modulated ground states, and it has been reported in Ref. [53]. Apart from the presence of a vortex in the center of the stripe, the structure is different from the ideal 1D nonflat spiral in that (a) $\boldsymbol{n}$ tilts out of plane close to the stripe boundaries and (b) the spiral structure close to the stripe boundaries is different from that in the stripe center as seen in the vector plot. Indeed, edge (half) vortices are present at the boundaries of the stripe.

Further increasing the velocity, for large enough $\lambda$, we obtain a periodic chain of vortices with opposite polarities, as shown in Fig. 4(b). It appears that the edge vortices already present in Fig. 4(a) enter the stripe and develop into full vortices in Fig. 4(b). The transition from the nonflat spiral to the chain of vortices appears to be a discontinuous one. For example, in the transition between Figs. 4(a) and 4(b), one can see the sudden change in the periodicity of the structure. We have a phase transition to a lattice of topological solitons induced by the dynamics.

When the velocity exceeds the value $v_F(\lambda)$ in Eq. (10), we expect a flat spiral to develop. This actually happens close to $v = v_F(\lambda)$ for small $\lambda$ and for $v$ larger than $v_F(\lambda)$ for large $\lambda$. Figure 4(c) shows a flat spiral in the stripe. The vortex gets elongated across the width of the stripe and disappears from the configuration, while the component $n_2$ is nearly zero. As a result, the configuration is close to the 1D spiral, but

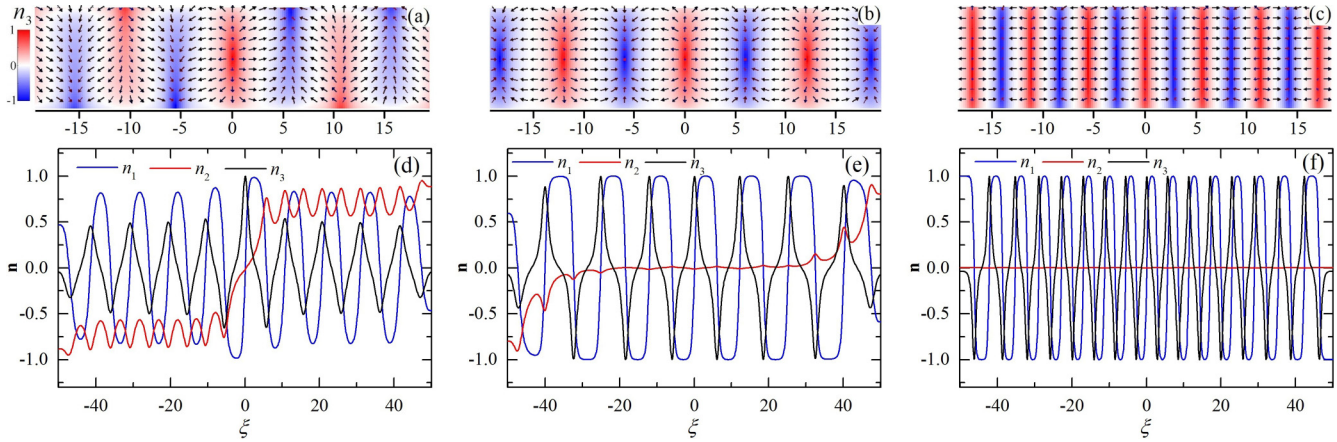


FIG. 4. Vector plots for parameter value $\lambda = 0.4$ for (a) a nonflat spiral at velocity $v = 0.78$, (b) a vortex chain at $v = 0.79$, and (c) a flat spiral at $v = 0.90$. Plotting conventions are as in Fig. 1. (d)–(f) The components of $\boldsymbol{n}$ along the line in the center of the stripe ($y = 0$) for the configurations shown in (a)–(c). The numerical mesh boundary, seen at $x = \pm 50$ in (e) and (f), has a negligible effect on the configurations in the lattice interior.

some dependence of $\boldsymbol{n}$ on $y$ is seen in the region close to the boundaries. The transition from the chain of vortices to the spiral appears to be a continuous one.

The nonflat spiral in Fig. 4(a) and the vortex chain in Fig. 4(b) are purely dynamical states, because they are solutions of Eq. (6), which does not have an equivalent form in the static case. This is confirmed also by the numerical simulations. Indeed, if we use these states as initial conditions and reduce the velocity to zero, they do not persist, and we obtain again the hybrid vortex. By contrast, since the flat spiral configuration does not depend on the $y$ coordinate, Eq. (6) reduces to Eq. (7), which is equivalent to the 1D static case.

Figure 5 shows the numerically found velocities for the transitions to the nonflat spiral, the vortex chain, and the flat spiral for various values of the DMI parameter $\lambda$. The velocities $v_{NF}(\lambda)$ and $v_F(\lambda)$ are plotted with solid lines for comparison.

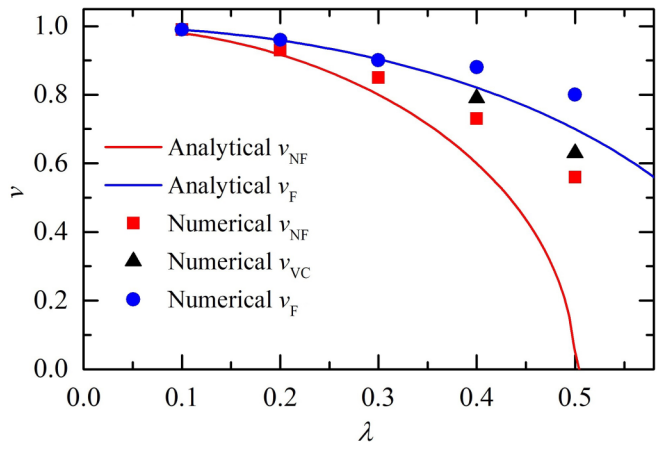


FIG. 5. The points mark the numerically found velocities for the transition to the nonflat spiral (red squares), to the vortex chain (black triangles), and to the flat spiral (blue circles) for various values of $\lambda$. The red solid line shows the velocity $v_{NF}(\lambda)$ of Eq. (8), and the blue solid line shows $v_F(\lambda)$ of Eq. (10), for comparison with the numerical results.

Regarding the transition to the nonflat spiral, we attribute the deviations from the expected transition velocity to the 2D nature of the structure explained in connection with Fig. 4(a). In a more quantitative argument, the boundary conditions favor the orientation of $\boldsymbol{n}$ in the $\hat{\boldsymbol{e}}_2$ direction over the orientation of $\boldsymbol{n}$ in the $\hat{\boldsymbol{e}}_1$ direction, and it is therefore expected that the Néel state will persist longer, compared with the 1D model, before it is destabilized to the nonflat spiral. Regarding the transition to the flat spiral, this is happening at $v$ larger than $v_F$ clearly due to the appearance of an additional state, that is, the vortex chain. For small $\lambda$, no vortex chain is formed because the transition to the nonflat spiral occurs at a high velocity $v \approx v_{NF}$, where the vortex is very elongated.

## V. CONCLUDING REMARKS

We have studied vortices and their dynamics in an antiferromagnet with easy-plane anisotropy and interfacial DMI. We have considered a nanostripe geometry and applied a continuum model. The stripe boundary induces a quasiuniform ground state with the Néel vector lying primarily perpendicular to the boundary. The form of the ground state forces the vortex to have a hybrid character with both Néel and Bloch chirality.

A vortex may propagate freely up to a maximum velocity that is smaller than the spin wave velocity. This is explained by theoretical arguments that lead to the general result that the velocity of localized excitations in chiral AFMs cannot reach the spin wave velocity. When the vortex is forced beyond the maximum velocity, it gives rise to phase transitions to a nonflat spiral, a vortex chain, and a flat spiral successively as the velocity increases. While the spiral phases are anticipated by a study of the 1D model, the vortex chain is a feature of the stripe geometry. This should be contrasted with the report that no vortex lattice has been found in this system in an infinite film [40].

## ACKNOWLEDGMENTS

This work was supported by the project "ThunderSKY" funded by the Hellenic Foundation for Research and Innova-

tion and the General Secretariat for Research and Technology, under Grant No. 871. We are grateful to M. Plexousakis for discussions on the numerical algorithms and to J. Chovan for a number of useful remarks on the text.

## APPENDIX A: ONE-DIMENSIONAL SYSTEM WITH BOUNDARIES

We assume a one-dimensional system of length $w$; specifically, we consider a time-independent Néel vector $\boldsymbol{n} = \boldsymbol{n}(y)$ in the interval $-w/2 \leqslant y \leqslant w/2$. This satisfies a reduced form of Eq. (2) of the main text,

$$\boldsymbol{n} \times (\boldsymbol{n}'' + 2\lambda \hat{\boldsymbol{e}}_1 \times \boldsymbol{n}' - n_3 \hat{\boldsymbol{e}}_3) = 0, \tag{A1}$$

where the prime denotes differentiation with respect to $y$. The equation is supplemented with the boundary condition

$$\boldsymbol{n}' + \lambda \hat{\boldsymbol{e}}_1 \times \boldsymbol{n} = 0, \quad y = \pm \frac{w}{2}. \tag{A2}$$

We are looking for the ground state of this system.

An obvious solution of Eq. (A1) is $\boldsymbol{n} = \hat{\boldsymbol{e}}_1$, and this also satisfies the boundary condition. Its energy is $E = 0$.

A state with negative energy can be found if we write

$$n_1 = 0, \quad n_2 = \cos\Theta, \quad n_3 = \sin\Theta, \tag{A3}$$

where we use the parametrization with the polar angle $\Theta$ measured from the $\hat{\boldsymbol{e}}_2$ direction. Equation (1) of the main text for the energy reduces to the form

$$V = \frac{1}{2}\int (\Theta')^2\, dy + \frac{1}{2}\int \sin^2\Theta\, dy + \lambda \int \Theta'\, dy, \tag{A4}$$

where the integrations extend over the interval $-w/2 \leqslant y \leqslant w/2$.

Energy minimization, $\delta E/\delta\Theta = 0$, gives

$$(\Theta')^2 = \sin^2\Theta + \gamma^2, \tag{A5}$$

where $\gamma$ is a constant. The boundary condition is

$$\frac{\delta V}{\delta \Theta'} = 0 \Rightarrow \Theta' = -\lambda, \quad y = \pm\frac{w}{2}, \tag{A6}$$

and coincides with (A2). In the present problem, we will assume $\boldsymbol{n}(y=0) = \pm\hat{\boldsymbol{e}}_2$ in the center of the interval (the solution will be symmetric with respect to the center). Thus we confine the problem in the interval $0 \leqslant y \leqslant w/2$, and we are seeking solutions with the boundary conditions

$$\Theta(y=0) = 0, \pi, \quad \Theta'\left(y = \pm\tfrac{w}{2}\right) = -\lambda. \tag{A7}$$

For the case $\Theta(y=0) = 0$, Eq. (A5) has the implicit solution

$$y = -\int_0^{\Theta} \frac{d\theta}{\sqrt{\sin^2\theta + \gamma^2}}, \tag{A8}$$

where we have chosen the case $\Theta' < 0$ and thus $\Theta(y)$ is a monotonically decreasing function of $y$. Figure 6 shows the components of $\boldsymbol{n}$ found numerically by solving Eq. (A1), for two values of the system length $w$. We have a tilting of the Néel vector out of plane near the edges of the system. The system is symmetric with respect to the transformation $\boldsymbol{n} \to -\boldsymbol{n}$. The two equivalent solutions will be denoted by $\boldsymbol{n}_\pm$.

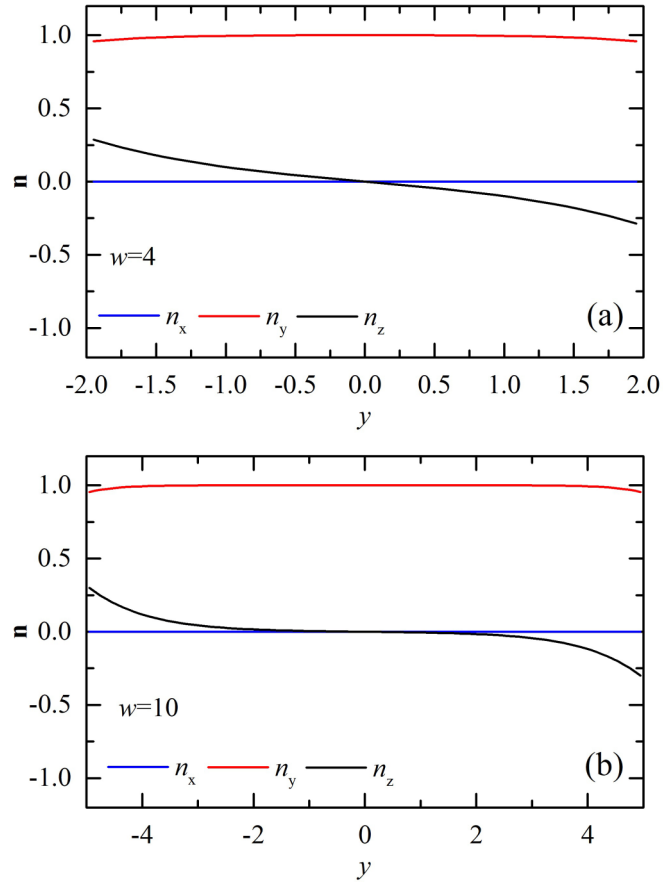


FIG. 6. The ground state obtained as the solution of Eq. (A1) for the boundary conditions in Eq. (A2) for system lengths (a) $w = 4$ and (b) $w = 10$. A second solution is obtained by $\boldsymbol{n} \to -\boldsymbol{n}$. We denote these two states by $\boldsymbol{n}_\pm$.

A remark of significant practical importance regarding the numerical application of the boundary conditions is the following. We have found the solutions of (A1) by using the boundary conditions (A2) and also by using open boundary conditions inspired by the physical problem. In the latter case, the edge spins have only one neighbor. The result for the states $\boldsymbol{n}_\pm$ is the same in both cases indicating that the two boundary conditions are equivalent (as shown in Appendix C). This could be anticipated as the natural boundary conditions are indeed derived in order to describe free edges of the material.

We further denote

$$\Theta'(y=0) = \gamma, \quad \Theta\left(y = \pm\tfrac{w}{2}\right) = \mp\Theta_w, \pi \mp \Theta_w. \tag{A9}$$

At the boundaries, $y = \pm w/2$, Eq. (A5) gives the tilting angle $\Theta_w$,

$$\sin^2\Theta_w = \lambda^2 - \gamma^2. \tag{A10}$$

This also implies that $|\gamma| < \lambda$.

In the case of a *narrow stripe,* the angle is $|\Theta| \ll 1$ for all $y$ [assume the case $\Theta(y=0) = 0$]. Equation (A8) gives

$$\Theta(y) = -\gamma y + O(y^3).$$

To the same order of approximation, we have $\gamma \approx \lambda$ and

$$\Theta(y) \approx -\lambda y. \tag{A11}$$

The maximum angle, attained at the boundary, is $\Theta_w = \lambda w/2$. The condition for the validity of the result is $\lambda w \ll \gamma \Rightarrow w \ll 1$. The energy (A4) has the value

$$V = -\frac{\lambda^2}{2} w, \quad w \ll 1. \tag{A12}$$

In the case of a *wide stripe,* we assume that the configuration is almost uniform in the center, $\sin\Theta = 0$, $\Theta' = 0$. We set $\gamma = 0$ in Eq. (A5), and this reduces to

$$(\Theta')^2 = \sin^2\Theta. \tag{A13}$$

Equation (A13) has the domain wall solution

$$\tan\frac{\Theta}{2} = -e^{y-y_0}, \tag{A14}$$

where $y_0$ is a constant. The Néel vector components are

$$n_2 = -\tanh(y - y_0), \quad n_3 = -\mathrm{sech}(y - y_0). \tag{A15}$$

The constant $y_0$ is determined by the boundary conditions (A6),

$$\Theta'(y = \pm\tfrac{w}{2}) = -\lambda \Rightarrow \mathrm{sech}\left(\pm\tfrac{w}{2} - y_0\right) = \lambda. \tag{A16}$$

At the boundaries, $\Theta'(\pm w/2) = -\lambda < 1/2$; thus $|y_0| > w/2$ (that is, the center of the domain wall solution is beyond the boundary). The form (A15) applies to Fig. 6 for $w = 10$.

We will now prove that the energy for all $\boldsymbol{n}_\pm$ is $V < 0$. For $0 \leqslant \Theta \leqslant \pi/2$, Eq. (A5) gives that $|\Theta'|$ is an increasing function of $\Theta$ and thus also an increasing function of $y$. We have $|\Theta'(y)| \leqslant \lambda$ with the maximum value attained at the boundary, $|\Theta'(y = w/2)| = \lambda$. We insert Eq. (A5) into Eq. (A4) and then use the inequality for $|\Theta'|$ to find that the energy of the configuration is negative,

$$V \leqslant \int (\Theta')^2\, dy + \lambda \int \Theta'\, dy < 0, \tag{A17}$$

where we take into account that $\Theta' < 0$. Equation (A17) establishes that the nonuniform states $\boldsymbol{n}_\pm$ have an energy lower than any uniform state in the system. They are found numerically to be the lowest energy states.

Figure 7 shows the energy of the ground states $\boldsymbol{n}_\pm$ as a function of the system length $w$. The dependence is linear for small $w$, following Eq. (A12), and it saturates to a negative value for larger $w$.

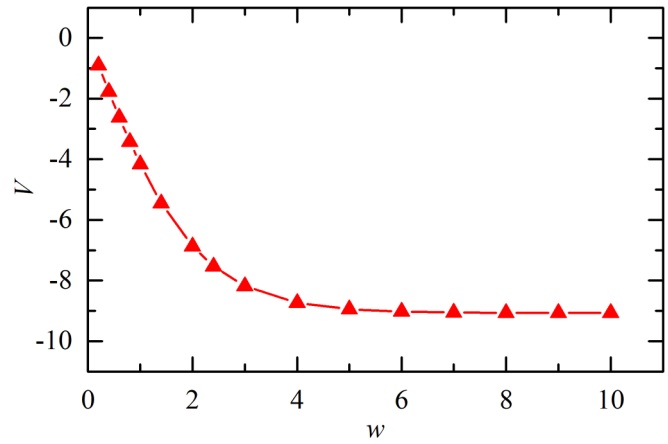


FIG. 7. Energy $V$ of the ground states $\boldsymbol{n}_\pm$ as a function of the system length $w$ for $\lambda = 0.3$. Symbols show numerical results connected by a solid line. The slope of the curve for small $w$ is given by Eq. (A12).

## APPENDIX B: PROPAGATING DOMAIN WALL

Let us consider the 1D system that results from Eq. (2) of the main text when we assume $\boldsymbol{n} = \boldsymbol{n}(x, t)$,

$$\boldsymbol{n} \times (\ddot{\boldsymbol{n}} - \boldsymbol{n}'' + 2\lambda\hat{\boldsymbol{e}}_2 \times \boldsymbol{n}' + n_3\hat{\boldsymbol{e}}_3), \tag{B1}$$

where the prime denotes differentiation with respect to $x$. Denote by

$$\boldsymbol{n}_{\mathrm{DW}}(x) = (\mathrm{sech}(x), 0, \tanh(x))$$

the static domain wall solution. This is stable for $\lambda < \lambda_{NF} = \frac{1}{2}$, while for $\lambda > \lambda_{NF}$ it is destabilized to the nonflat spiral.

A domain wall propagating with velocity $v$ satisfies

$$\boldsymbol{n} \times [(1 - v^2)\boldsymbol{n}'' - 2\lambda\hat{\boldsymbol{e}}_2 \times \boldsymbol{n}' - n_3\hat{\boldsymbol{e}}_3] = 0. \tag{B2}$$

The solution of the equation is obtained by a Lorentz transformation of the static wall

$$\boldsymbol{n}(x, t; v) = \boldsymbol{n}_{\mathrm{DW}}\left(\frac{x - vt}{\sqrt{1 - v^2}}\right).$$

Note that the DM term vanishes for the static or propagating domain wall solutions and thus Lorentz invariance is preserved. The propagating solution is valid for the range of parameter values where the Néel state is stable,

$$\frac{\lambda}{\sqrt{1 - v^2}} < \lambda_{NF} \Rightarrow v < \sqrt{1 - \left(\frac{\lambda}{\lambda_{NF}}\right)^2} \equiv v_0. \tag{B3}$$

As the velocity increases, the domain wall is contracted by a factor $\sqrt{1 - v^2}$, and it has a minimum width at $v = v_0$. For $v > v_0$ the propagating domain wall is unstable, and the system should turn into a propagating spiral state.

## APPENDIX C: OPEN AND NATURAL BOUNDARY CONDITIONS

We consider a vector field $\boldsymbol{n} = \boldsymbol{n}(x, t)$ with components $\boldsymbol{n} = (n_1, n_2, n_3)$ and a constant length $|\boldsymbol{n}| = 1$. It satisfies the equation

$$\boldsymbol{n} \times (\boldsymbol{n}'' + 2\lambda\hat{\boldsymbol{e}}_2 \times \boldsymbol{n}' - n_3\hat{\boldsymbol{e}}_3) = 0, \tag{C1}$$

where $\lambda$ is a parameter. The problem is defined in an interval $-w/2 \leqslant x \leqslant w/2$, and the boundary conditions (so-called *natural boundary conditions*) are

$$\boldsymbol{n}' + \lambda\hat{\boldsymbol{e}}_2 \times \boldsymbol{n} = 0, \quad x = \pm\frac{w}{2}. \tag{C2}$$

We discretize space and have a lattice of points $x_i$, $i = 1, \ldots, N$ with lattice spacing $a$. On the lattice, the discrete version of Eq. (C1) reads

$$\boldsymbol{n}_i \times \left(\frac{\boldsymbol{n}_{i+1} + \boldsymbol{n}_{i-1}}{a^2} + \lambda\hat{\boldsymbol{e}}_2 \times \frac{\boldsymbol{n}_{i+1} - \boldsymbol{n}_{i-1}}{a} - n_{i,3}\hat{\boldsymbol{e}}_3\right) = 0 \tag{C3}$$

for any site $i = 1, \ldots, N$ of the lattice with lattice spacing $a$.

We consider the following two approaches for implementing the boundary conditions.

(*a*) *Open boundary conditions.* Motivated by the physical problem, we use open boundary conditions (that is, we assume that there is no interaction to the right of the last site, $i = N$), and thus Eq. (C3) gives at the last site, $i = N$,

$$\boldsymbol{n}_N \times \left( \frac{\boldsymbol{n}_{N-1}}{a^2} - \lambda \hat{\boldsymbol{e}}_2 \times \frac{\boldsymbol{n}_{N-1}}{a} - n_{N,3} \hat{\boldsymbol{e}}_3 \right) = 0. \tag{C4}$$

A similar equation is obtained for the first site, $i = 1$.

(*b*) *Applying boundary conditions to order* $O(a)$. The discrete form of (C2) at $i = N$ reads

$$\frac{\boldsymbol{n}_{N+1} - \boldsymbol{n}_N}{a} + \lambda \hat{\boldsymbol{e}}_2 \times \boldsymbol{n}_{N+1} = 0$$
$$\Rightarrow \frac{\boldsymbol{n}_{N+1}}{a} + \lambda \hat{\boldsymbol{e}}_2 \times \boldsymbol{n}_{N+1} = \frac{\boldsymbol{n}_N}{a}, \tag{C5}$$

correct to order $O(a)$. The latter can be used in Eq. (C3) to give (C4). This proves the equivalence of the open boundary conditions with the natural boundary conditions.


[1] T. Jungwirth, X. Marti, P. Wadley, and J. Wunderlich, Antiferromagnetic spintronics, Nat. Nanotechnol. **11**, 231 (2016).

[2] V. Baltz, A. Manchon, M. Tsoi, T. Moriyama, T. Ono, and Y. Tserkovnyak, Antiferromagnetic spintronics, Rev. Mod. Phys. **90**, 015005 (2018).

[3] P. Wadley, B. Howells, J. Elezny, C. Andrews, V. Hills, R. P. Campion, V. Novak, K. Olejnik, F. Maccherozzi, S. S. Dhesi, S. Y. Martin, T. Wagner, J. Wunderlich, F. Freimuth, Y. Mokrousov, J. Kune, J. S. Chauhan, M. J. Grzybowski, A. W. Rushforth, K. W. Edmonds *et al.*, Electrical switching of an antiferromagnet, Science **351**, 587 (2016).

[4] M. J. Grzybowski, P. Wadley, K. W. Edmonds, R. Beardsley, V. Hills, R. P. Campion, B. L. Gallagher, J. S. Chauhan, V. Novak, T. Jungwirth, F. Maccherozzi, and S. S. Dhesi, Imaging Current-Induced Switching of Antiferromagnetic Domains in CuMnAs, Phys. Rev. Lett. **118**, 057701 (2017).

[5] T. Moriyama, K. Oda, T. Ohkochi, M. Kimata, and T. Ono, Spin torque control of antiferromagnetic moments in NiO, Sci. Rep. **8**, 14167 (2018).

[6] S. Yu. Bodnar, M. Filianina, S. P. Bommanaboyena, T. Forrest, F. Maccherozzi, A. A. Sapozhnik, Y. Skourski, M. Kläui, and M. Jourdan, Imaging of current induced Néel vector switching in antiferromagnetic $Mn_2$ Au, Phys. Rev. B **99**, 140409(R) (2019).

[7] L. Baldrati, O. Gomonay, A. Ross, M. Filianina, R. Lebrun, R. Ramos, C. Leveille, F. Fuhrmann, T. R. Forrest, F. Maccherozzi, S. Valencia, F. Kronast, E. Saitoh, J. Sinova, and M. Kläui, Mechanism of Néel Order Switching in Antiferromagnetic Thin Films Revealed by Magnetotransport and Direct Imaging, Phys. Rev. Lett. **123**, 177201 (2019).

[8] J. Shi, V. Lopez-Dominguez, F. Garesci, C. Wang, H. Almasi, M. Grayson, G. Finocchio, and P. Khalili Amiri, Electrical manipulation of the magnetic order in antiferromagnetic PtMn pillars, Nat. Electron. **3**, 92 (2020).

[9] R. Cheng, M. W. Daniels, J.-G. Zhu, and D. Xiao, Ultrafast switching of antiferromagnets via spin-transfer torque, Phys. Rev. B **91**, 064423 (2015).

[10] P. E. Roy, R. M. Otxoa, and J. Wunderlich, Robust picosecond writing of a layered antiferromagnet by staggered spin-orbit fields, Phys. Rev. B **94**, 014439 (2016).

[11] V. Lopez-Dominguez, H. Almasi, and P. Khalili Amiri, Picosecond Electric-Field-Induced Switching of Antiferromagnets, Phys. Rev. Applied **11**, 024019 (2019).

[12] R. Cheng, D. Xiao, and A. Brataas, Terahertz Antiferromagnetic Spin Hall Nano-Oscillator, Phys. Rev. Lett. **116**, 207603 (2016).

[13] R. Khymyn, I. Lisenkov, V. Tiberkevich, B. A. Ivanov, and A. Slavin, Antiferromagnetic THz-frequency Josephson-like oscillator driven by spin current, Sci. Rep. **7**, 43705 (2017).

[14] V. Puliafito, R. Khymyn, M. Carpentieri, B. Azzerboni, V. Tiberkevich, A. Slavin, and G. Finocchio, Micromagnetic modeling of terahertz oscillations in an antiferromagnetic material driven by the spin Hall effect, Phys. Rev. B **99**, 024405 (2019).

[15] O. Gomonay, T. Jungwirth, and J. Sinova, High Antiferromagnetic Domain Wall Velocity Induced by Néel Spin-Orbit Torques, Phys. Rev. Lett. **117**, 017202 (2016).

[16] T. Shiino, S.-H. Oh, P. M. Haney, S.-W. Lee, G. Go, B.-G. Park, and K.-J. Lee, Antiferromagnetic Domain Wall Motion Driven by Spin-Orbit Torques, Phys. Rev. Lett. **117**, 087203 (2016).

[17] L. Sánchez-Tejerina, V. Puliafito, P. Khalili Amiri, M. Carpentieri, and G. Finocchio, Dynamics of domain-wall motion driven by spin-orbit torque in antiferromagnets, Phys. Rev. B **101**, 014433 (2020).

[18] X. Zhang, Y. Zhou, and M. Ezawa, Antiferromagnetic skyrmion: Stability, creation and manipulation, Sci. Rep. **6**, 24795 (2016).

[19] J. Barker and O. A. Tretiakov, Static and Dynamical Properties of Antiferromagnetic Skyrmions in the Presence of Applied Current and Temperature, Phys. Rev. Lett. **116**, 147203 (2016).

[20] O. Gomonay, V. Baltz, A. Brataas, and Y. Tserkovnyak, Antiferromagnetic spin textures and dynamics, Nat. Phys. **14**, 213 (2018).

[21] A. Salimath, F. Zhuo, R. Tomasello, G. Finocchio, and A. Manchon, Controlling the deformation of antiferromagnetic skyrmions in the high-velocity regime, Phys. Rev. B **101**, 024429 (2020).

[22] B. A. Ivanov and D. D. Sheka, Dynamics of Vortices and Their Contribution to the Response Functions of Classical Quasi-Two-Dimensional Easy-Plane Antiferromagnet, Phys. Rev. Lett. **72**, 404 (1994).

[23] A. R. Pereira and A. S. T. Pires, Dynamics of vortices in a two-dimensional easy-plane antiferromagnet, Phys. Rev. B **51**, 996 (1995).

[24] B. A. Ivanov, A. K. Kolezhuk, and G. M. Wysin, Normal Modes and Soliton Resonance for Vortices in 2D Classical Antiferromagnets, Phys. Rev. Lett. **76**, 511 (1996).

[25] A. Bogdanov and A. Shestakov, Vortex states in antiferromagnetic crystals, Phys. Solid State **40**, 1350 (1998).

[26] S. Komineas and N. Papanicolaou, Vortex dynamics in two-dimensional antiferromagnets, Nonlinearity **11**, 265 (1998).

[27] J. Wu, D. Carlton, J. S. Park, Y. Meng, E. Arenholz, A. Doran, A. T. Young, A. Scholl, C. Hwang, H. W. Zhao, J. Bokor, and Z. Q. Qiu, Direct observation of imprinted antiferromagnetic vortex states in CoO/Fe/Ag(001) discs, Nat. Phys. **7**, 303 (2011).

[28] F. P. Chmiel, N. Waterfield Price, R. D. Johnson, A. D. Lamirand, J. Schad, G. van der Laan, D. T. Harris, J. Irwin, M. S. Rzchowski, C.-B. Eom, and P. G. Radaelli, Observation of magnetic vortex pairs at room temperature in a planar $\alpha$-$Fe_2O_3$/Co heterostructure, Nat. Mater. **17**, 581 (2018).

[29] H. Jani, J.-C. Lin, J. Chen, J. Harrison, F. Maccherozzi, J. Schad, S. Prakash, C.-B. Eom, A. Ariando, T. Venkatesan, and P. G. Radaelli, Antiferromagnetic half-skyrmions and bimerons at room temperature, Nature (London) **590**, 74 (2021).

[30] M. E. Gouvêa, G. M. Wysin, A. R. Bishop, and F. G. Mertens, Vortices in the classical two-dimensional anisotropic Heisenberg model, Phys. Rev. B **39**, 11840 (1989).

[31] N. Papanicolaou and P. N. Spathis, Semitopological solitons in planar ferromagnets, Nonlinearity **12**, 285 (1999).

[32] T. Shinjo, T. Okuno, R. Hassdorf, K. Shigeto, and T. Ono, Magnetic vortex core observation in circular dots of permalloy, Science **289**, 930 (2000).

[33] A. Wachowiak, J. Wiebe, M. Bode, O. Pietzsch, M. Morgenstern, and R. Wiesendanger, Direct observation of internal spin structure of magnetic vortex cores, Science **298**, 577 (2002).

[34] B. Van Waeyenberge, A. Puzic, H. Stoll, K. W. Chou, T. Tyliszczak, R. Hertel, M. Fähnle, H. Brückl, K. Rott, G. Reiss, I. Neudecker, D. Weiss, C. H. Back, and G. Schütz, Magnetic vortex core reversal by excitation with short bursts of an alternating field, Nature (London) **444**, 461 (2006).

[35] K. Yamada, S. Kasai, Y. Nakatani, K. Kobayashi, H. Kohno, A. Thiaville, and T. Ono, Electrical switching of the vortex core in a magnetic disk, Nat. Mater. **6**, 269 (2007).

[36] V. S. Pribiag, I. N. Krivorotov, G. D. Fuchs, P. M. Braganca, O. Ozatay, J. C. Sankey, D. C. Ralph, and R. A. Buhrman, Magnetic vortex oscillator driven by dc spin-polarized current, Nat. Phys. **3**, 498 (2007).

[37] S. Komineas, Rotating Vortex Dipoles in Ferromagnets, Phys. Rev. Lett. **99**, 117202 (2007).

[38] S. Mühlbauer, S. N. Gvasaliya, E. Pomjakushina, and A. Zheludev, Double-$k$ phase of the Dzyaloshinskii-Moriya helimagnet $Ba_2CuFe_2O_7$, Phys. Rev. B **84**, 180406(R) (2011).

[39] S. Mühlbauer, S. Gvasaliya, E. Ressouche, E. Pomjakushina, and A. Zheludev, Phase diagram of the Dzyaloshinskii-Moriya helimagnet $Ba_2CuGe_2O_7$ in canted magnetic fields, Phys. Rev. B **86**, 024417 (2012).

[40] J. Chovan, N. Papanicolaou, and S. Komineas, Intermediate phase in the spiral antiferromagnet $Ba_2CuGe_2O_7$, Phys. Rev. B **65**, 064433 (2002).

[41] J. Chovan and N. Papanicolaou, Commensurate and incommensurate magnetism in layered antiferromagnets, in *Frontiers in Magnetic Materials*, edited by A. V. Narlikar (Springer, Berlin, 2005), pp. 347–384.

[42] A. N. Bogdanov and A. Hubert, The stability of vortex-like structures in uniaxial ferromagnets, J. Magn. Magn. Mater. **195**, 182 (1999).

[43] S. Komineas and N. Papanicolaou, Traveling skyrmion in chiral antiferromagnets, SciPost Phys. **8**, 086 (2020).

[44] I. V. Baryakhtar and B. A. Ivanov, Nonlinear magnetization waves of an antiferromagnet, Sov. J. Low Temp. Phys. **5**, 361 (1979).

[45] R. Tomasello, L. Sanchez-Tejerina, V. Lopez-Dominguez, F. Garescì, A. Giordano, M. Carpentieri, P. K. Amiri, and G. Finocchio, Domain periodicity in an easy-plane antiferromagnet with Dzyaloshinskii-Moriya interaction, Phys. Rev. B **102**, 224432 (2020).

[46] H. Jani, J. Linghu, S. Hooda, R. V. Chopdekar, C. Li, G. J. Omar, S. Prakash, Y. Du, P. Yang, A. Banas, K. Banas, S. Ghosh, S. Ojha, G. R. Umapathy, D. Kanjilal, A. Ariando, S. J. Pennycook, E. Arenholz, P. G. Radaelli, J. M. D. Coey *et al.*, Reversible hydrogen control of antiferromagnetic anisotropy in $\alpha$-$Fe_2O_3$, Nat. Commun. **12**, 1668 (2021).

[47] A. Thiaville, S. Rohart, É. Jué, V. Cros, and A. Fert, Dynamics of Dzyaloshinskii domain walls in ultrathin magnetic films, EPL (Europhys. Lett.) **100**, 57002 (2012).

[48] F. Büttner, I. Lemesh, and G. S. D. Beach, Theory of isolated magnetic skyrmions: From fundamentals to room temperature applications, Sci. Rep. **8**, 4464 (2018),

[49] P. Olleros-Rodríguez, R. Guerrero, J. Camarero, O. Chubykalo-Fesenko, and P. Perna, Intrinsic mixed Bloch-Néel character and chirality of skyrmions in asymmetric epitaxial trilayers, ACS Appl. Mater. Interfaces **12**, 25419 (2020).

[50] A. Yu Aladyshkin, A. V. Silhanek, W. Gillijns, and V. V. Moshchalkov, Nucleation of superconductivity and vortex matter in superconductor–ferromagnet hybrids, Supercond. Sci. Technol. **22**, 053001 (2009).

[51] A. Kubetzka, J. M. Bürger, R. Wiesendanger, and K. von Bergmann, Towards skyrmion-superconductor hybrid systems, Phys. Rev. Materials **4**, 081401(R) (2020).

[52] A. P. Petrović, M. Raju, X. Y. Tee, A. Louat, I. Maggio-Aprile, R. M. Menezes, M. J. Wyszyński, N. K. Duong, M. Reznikov, Ch. Renner, M. V. Milošević, and C. Panagopoulos, Skyrmion-(Anti)Vortex Coupling in a Chiral Magnet-Superconductor Heterostructure, Phys. Rev. Lett. **126**, 117205 (2021).

[53] J. Chovan, M. Marder, and N. Papanicolaou, Weak ferromagnetism in the helimagnet $Ba_2CuGe_2O_7$, Acta Phys. Pol., A **126**, 32 (2004).